



HAL
open science

Nano-squares and regular LIPSS on YSZ coating by picosecond UV laser beam: Thin film mediated and direct texturing

Wael Karim, Agnès Petit, Eric Millon, Julien Vulliet, Malek Tabbal,
Anne-Lise Thomann, Nadjib Semmar

► To cite this version:

Wael Karim, Agnès Petit, Eric Millon, Julien Vulliet, Malek Tabbal, et al.. Nano-squares and regular LIPSS on YSZ coating by picosecond UV laser beam: Thin film mediated and direct texturing. *Applied Surface Science*, 2023, 623, pp.157110. 10.1016/j.apsusc.2023.157110 . hal-04056146

HAL Id: hal-04056146

<https://hal.science/hal-04056146v1>

Submitted on 4 Dec 2023

HAL is a multi-disciplinary open access archive for the deposit and dissemination of scientific research documents, whether they are published or not. The documents may come from teaching and research institutions in France or abroad, or from public or private research centers.

L'archive ouverte pluridisciplinaire **HAL**, est destinée au dépôt et à la diffusion de documents scientifiques de niveau recherche, publiés ou non, émanant des établissements d'enseignement et de recherche français ou étrangers, des laboratoires publics ou privés.

Nano-squares and regular LIPSS on YSZ coating by picosecond UV laser beam: thin film mediated and direct texturing

Wael Karim¹, Agnès Petit¹, Eric Millon¹, Julien Vulliet², Malek Tabbal³, Anne-lise Thomann¹, Nadjib Semmar^{1,*}

¹GREMI-UMR 7344-CNRS-University of Orleans, 14 Rue d'Issoudun, BP 6744, 45067 Orléans Cedex, France

²CEA DAM, Le Ripault, Place Raoul Dautry, 37250 Monts, France

³Department of Physics, American University of Beirut, Beirut 1107 2020, Lebanon

**Corresponding author:*
nadjib.semmar@univ-orleans.fr

Abstract

The laser texturing of high bandgap ceramic materials, such as Yttrium Stabilized Zirconia (YSZ), is very challenging due to their structural complexity, their mechanical fragility as well as the risk of a chemical decomposition under laser irradiation. The objective of this paper is to fabricate, in a controlled manner, well-organized nanostructures on microscale undulating YSZ coatings, and thus evaluate the feasibility to form laser-induced periodic surface structures (LIPSS), via two experimental approaches: the first one consists in laser structuring of YSZ through a mediated thin film (gadolinium doped ceria ~ 700 nm or Au ~20 nm), while the second one involves the direct structuring of the YSZ surface under static and scanning modes. A picosecond Nd: YAG laser (355 nm, 40 ps, 10 Hz) with a relatively large laser beam spot (~550 μm) was used. In the GDC and Au mediated texturing of YSZ under static conditions, we have observed nano-squares (~250 nm) and typical LIPSS perpendicular to the laser beam polarization, respectively. In the case of laser irradiation of the bare YSZ surface for fluences higher than $310 \pm 10 \text{ mJ/cm}^2$, LSFL and HSFL structures were formed depending on the number of pulses (from 10^2 to 10^3). The average spatial period measured for the thus-obtained HSFL is about 136 nm with an amplitude of 40 nm, as determined by Scanning Electron Microscopy (SEM) and Atomic Force Microscope (AFM). We have also demonstrated the ability to reproduce LIPSS on YSZ under scanning mode. A "darkening" phenomenon was observed on the YSZ surface at laser fluences exceeding 600 mJ/cm^2 , resulting from the formation of micro-spikes (with sizes close to 1 μm). XRD measurements demonstrated a slightly lower crystallinity of the laser irradiated YSZ material compared to the untreated YSZ surface.

Keywords: Yttrium-stabilized zirconia; picosecond laser beam; Nano-structuring; LIPSS; Laser darkening.

1. Introduction

Ceramic oxide materials have several attractive properties such as good thermal resistance, high hardness values in addition to being, in many instances, chemically stable and biocompatible [1]. They have been used in the aerospace and automotive industries [2,3], as well as in the biomedical field [4,5]. Among such ceramics is the complex oxide yttrium-stabilized zirconia (YSZ) which is currently used as an electrolyte in solid oxide electrochemical cells (SOEC) for hydrogen production through high temperature electrolysis processes [6-8]. For such applications, it is beneficial to increase the exchange surface area of the electrolyte /electrode interface. This can be done through the nano/micro-structuring of the surface of the YSZ electrolyte. Texturing of ceramic surfaces can be achieved through plasma etching [9] Computer Numerical Control (CNC) micromachining [10], or laser-based processes, such as thermal ablation and Direct Laser Interference Patterning (DLIP). One alternative laser-based approach is irradiation of the sample's surface slightly below the laser ablation threshold to form Laser Induced Periodic Structures (LIPSS) [11]. Such structures can be formed on different types of materials in a controlled manner and, under appropriate conditions, at nanoscale dimensions. As far as wide band-gap dielectric materials are concerned, it has indeed recently been shown that sub-picosecond laser beams could be used to obtain nanoscale LIPSS with periods depending on the wavelength " λ " of the laser beam. Dufft et al [12] detected on zinc oxide (ZnO) two types of LIPSS, Low Spatial Frequency (LSFL) LIPSS with a period $\Lambda \approx \lambda$ and High Spatial Frequency (HSFL) LIPSS with $\lambda/2 < \Lambda < \lambda$, by using a femto-second laser beam at 800 nm with laser fluence values ranging from 0.7 to 0.8 J/cm² (for LSFL) and from 0.5 to 0.7 J/cm² (for HSFL). On the other hand, Bashir et al [13] obtained HSFL structures, having a period of 70 nm on the surface of calcium fluoride (CaF₂, a wide band-gap dielectric), by irradiation with a femto-second laser beam at 800 nm with a fluence of 0.5 J/cm², a value that is very close to the ablation threshold of CaF₂. Furthermore, the LSFL structures have been observed only on the metallic phase (Nb) of the composite alumina-zirconia-niobium Al₂O₃ - ZrO₂ - Nb (78.3 - 1.7 - 20 vol%), by means of a femto-second laser at 1025 nm [14], with a laser fluence of 0.4 J/cm², which exceeds the ablation threshold of niobium (0.19 J/cm²) [15], while no chemical and morphological changes were detected on the surface of the ceramic material, since 0.4 J/cm² is well below the ablation threshold of Al₂O₃ ($F_{th} = 5.62$ J/cm²) [16], keeping in mind that the band-gap of Al₂O₃ is 7 eV [16].

Unlike metals and commonly used semiconductors, the absorption of a UV picosecond laser beam (355 nm) by wide bandgap materials, such as yttria-stabilized zirconia "YSZ" ($E_{gap} = 5,8$ eV) [16], is less efficient compared to the femtosecond case, due to the transparent nature of the material and the limited multiphoton ionization and tunneling phenomena [17] at typical picosecond laser intensities ($\sim 10^9$ W/cm²). Thus, higher laser intensities are needed to work near the ablation threshold to induce LIPSS formation but simultaneously this would lead to enhanced damage formation in such fragile ceramic materials, and thus subsequently reduces the process window. To circumvent such limitations, it has been shown that the deposition of a thin metallic film on the substrate surface prior to laser structuring was beneficial either for lowering the threshold of LIPSS formation on dielectrics and semiconductors or to directly structuring the irradiated thin films by ultrashort beams [18-27]. For example, Liu et al [28] have achieved HSFL fine structures (period ~ 100 nm) on the surface of ZnO assisted by aluminum film after femtosecond laser processing at 800 nm and 120 fs. The ablation threshold F_{th} was decreased by about 54%, compared to the uncoated pristine sample of ZnO. Clemens et al [29] showed the generation of LIPSS on large areas of fused silica using a thin layer of gold and a femtosecond laser at 1025 nm with a pulse duration of 300 fs. The thin metal layer enhances the coupling of the laser beam with the underlying substrate through Surface Plasmons Polaritons (SPP) waves. As widely discussed in both theoretical and experimental works [30,31], the interference of the latter with

the incident laser beam initiates LIPSS formation.

In the context of SOEC optimization, we previously investigated the laser texturing of a Gadolinium Doped Ceria (GDC) thin layer on the YSZ to enhance electrode surface area [32]. The GDC layer was introduced as a diffusion barrier layer to inhibit the formation of undesired oxide phases that may be detrimental to the cell's performance [33]. In that work [32], a UV picosecond beam was utilized and LIPSS pattern on GDC were formed depending on laser dose (defined as the laser fluence times the number of pulses, $F \times N$). It was also reported that, at high laser doses, ablation of the entire GDC film can take place leaving a textured YSZ substrate, in the form of nano-squared structures. Based on this finding, the present paper is dedicated to the investigation of the texturing of YSZ using the same UV laser beam under various configurations. First, we will consider the laser irradiation of the YSZ surface coated by the GDC layer, as is the case in a real SOEC. Then, we will investigate the effect of the presence of a metal coating, namely Au, on the laser irradiation of YSZ. Finally, we will compare the results of these experiments with the laser structuring of the bare YSZ surface under both static and scanning mode configurations. At last, we explore the effect of increasing the laser dose leading to the formation of nano and micro spikes.

2. Experimental

The YSZ substrates, $(\text{ZrO}_2)_{0.92}(\text{Y}_2\text{O}_3)_{0.08}$, provided by the 'Commissariat de l'Energie Atomique' (CEA), have thicknesses of about $8 \mu\text{m}$ and were deposited by screen-printing on a porous Ni-YSZ cermet, as shown in the Figure 1. This led to a somewhat undulating YSZ surface at the microscale (a few microns). Approximately 700 nm thick GDC thin films were deposited by pulsed direct current magnetron sputtering from a 4-inch diameter of $\text{Ce}_{1-x}\text{Gd}_x$ metal target onto the YSZ substrates. All deposition runs were performed at room temperature at a pressure of 1 Pa with 20 sccm Ar as sputtering gas, 2 sccm O_2 as a reactive gas. The as-deposited films were then annealed in air at $500 \text{ }^\circ\text{C}$, a process that resulted in highly crystalline and stoichiometric layers ($\text{Ce}_{1-x}\text{Gd}_x\text{O}_2$). More details on the growth conditions and properties of the films have been presented elsewhere by Mickan et al [33]. On the other hand, the Au thin films have a thickness of $\sim 20 \text{ nm}$ and were deposited on YSZ by plasma sputtering from a 2-inch gold target at a pressure of 0.5 Pa with 20 sccm Ar as sputtering gas.

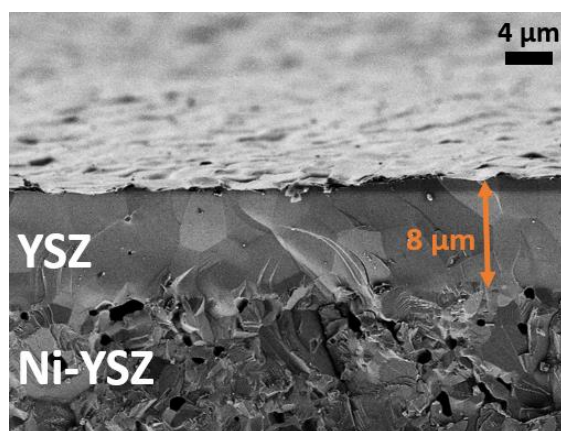


Fig.1 Scanning Electron Microscope image showing the transverse section of the YSZ substrate.

All irradiation experiments were performed using a picosecond Nd: YAG laser operating at its third harmonic ($\lambda = 355$ nm) with a pulse duration of 40 ps and a repetition rate of 10 Hz [32]. The energy/pulse is modulated using an optical filter energy (Thorlabs UGC), and the laser Gaussian beam is focused to a 550 μm diameter spot on the sample's surface using a quartz lens with a focal length of 75 mm. The samples were irradiated in static mode (by accumulation of successive shots) or in scanning mode in ambient air as shown in Figure 2. In static mode, the total number of shots (N) irradiating the same area of the sample is controlled by synchronized beam chopper. In scanning mode, which is necessary for large area irradiation, the sample is mounted on a motorized and computer-controlled X, Y scanning stage. To irradiate the entire film surface, an S-shaped scanning pattern of the sample is realized via a LabVIEW interface. Using an automated scanning system (Newport-Conex CC scanner with an accessible speed ranging from 0.001 to 5 mm/s in the X, Y directions, with a translation path $\Delta Y = 100$ μm), the sample is moved along the X-axis at a speed V_x and displaced by a distance ΔY (perpendicular to the X-axis) at the end of the movement.

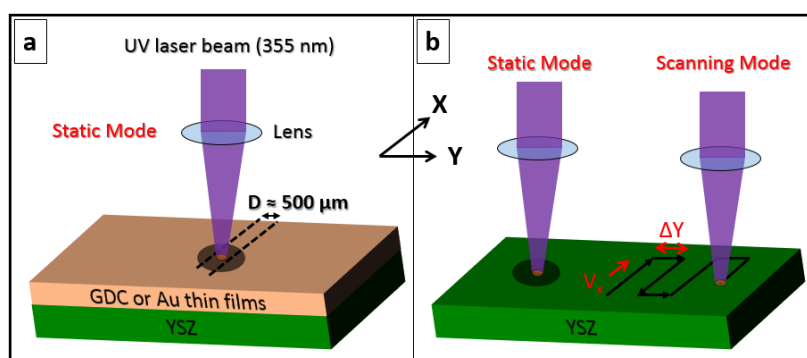


Fig.2 Schematics of mediated (a) and direct (b) structuring approaches for YSZ material.

For the present study, the laser fluence (F) and the pulse number (N) were typically varied from 125 to 375 mJ/cm^2 , and from 10 to 1000 shots, respectively. In instances where a higher laser dose was needed, F and N were increased to 625 mJ/cm^2 and 20000, respectively. The values of V_x used in this work were varied from 6 $\mu\text{m}/\text{s}$ up to 100 $\mu\text{m}/\text{s}$. The surface morphology of the thin films before and after laser irradiation was examined using a Carl Zeiss SMT SUPRA 40 very high resolution field emission gun scanning electron microscope (SEM). The amplitude and periodicity of the LIPSS patterns were determined using an atomic force microscope (AFM). AFM images were collected using a Bruker Dimension Icon in ScanAsyst air mode. The structural characterization was carried out by X-ray diffraction (XRD) in the Bragg-Brentano $\theta/2\theta$ geometry using a Bruker D8 Discover system with Cu K α radiation (0.15406 nm).

3. Results and Discussion

1. Thin film-mediated structuring of YSZ

In this section, we will first report on the laser structuring (in static mode) of the YSZ material coated with the GDC barrier layer, then compare these results with laser irradiation of YSZ coated with a thin 20 nm Au film. Figure 3 shows SEM images of GDC/YSZ samples irradiated at different laser fluences and number of pulses. For low doses ($F=125 \pm 10$ mJ/cm^2 , $N=50$, Fig. 3.a), the sample's surface shows regularly arranged YSZ square shaped patterns or nano-squares (NS). These patterns are similar to the YSZ nano-squares observed at comparable laser doses reported in our previous work, where it was shown that this results from a complete ablation of the GDC film, as confirmed by Electron Dispersion X-Ray

(EDX) analyses [32]. These nanosquares are observed across the entire laser beam impact. Their size is close to the wavelength used at 355 nm, and their orientation is uniform within an YSZ grain but varies across grain boundaries. However, at higher laser doses ($F = 310 \pm 10 \text{ mJ/cm}^2$, $N = 1000$, Fig. 3.b), and within a single impact of the Gaussian laser beam, two different regions (Figs. 3.b1 and 3.b2) can be distinguished corresponding to the formation of two types of nanostructures. In order to estimate the fluence values between the edges and the center of the laser pattern, we have used the following an exponential function: $F(d) = F_0 e^{-(d/D)}$, with F_0 : Peak fluence at the point center; d : Beam of the zone concerned; D : laser spot beam $\approx 550 \mu\text{m}$.

Figure 3.b1 shows NS on YSZ substrate at the edge of laser spot that corresponds to the low intensity regions of the Gaussian beam ($F_{\text{Edges}} = 150 \text{ mJ/cm}^2$), in agreement with the low dose case presented in Fig. 3.a.

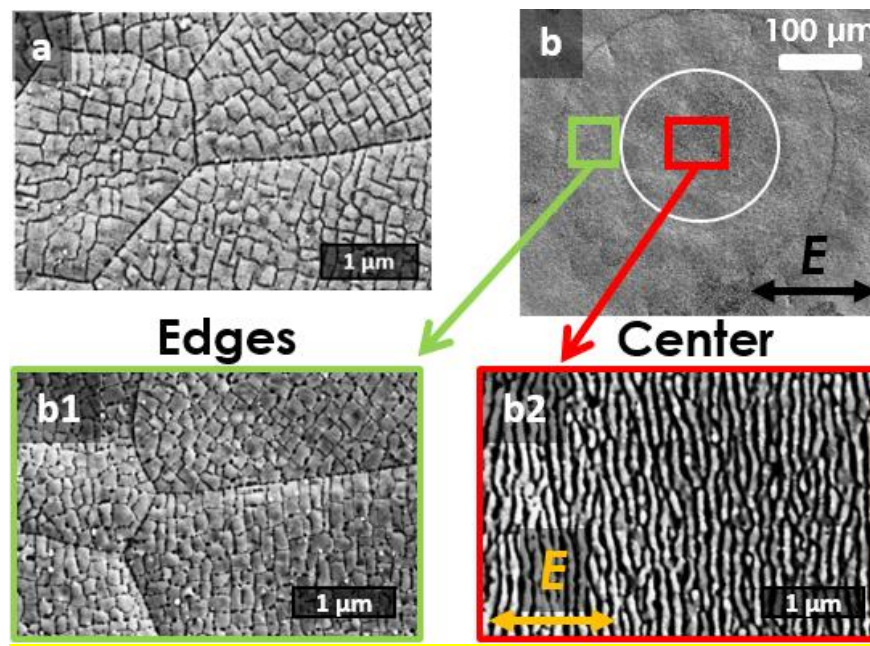


Fig.3 SEM images showing the comparison of the indirect texturing of YSZ at $F = 125 \text{ mJ/cm}^2$ and $N = 50$ (a) and $F = 310 \text{ mJ/cm}^2$ and $N = 1000$ (b) laser energy dose. The green box (b1) corresponds to the edges ($F_{\text{Edges}} = 150 \text{ mJ/cm}^2$) and the red box (b2) corresponds to the center ($F_{\text{Center}} \approx 215 \text{ mJ/cm}^2$) of laser spot presented in (b).

At the center of the beam, periodic ripples are observed on the YSZ substrate with a spatial period close to $110 \pm 10 \text{ nm}$ which is smaller than half the laser wavelength ($\lambda/2$). These ripples are thus identified as HSFL [16,34,35], oriented perpendicular to the E polarization of laser beam and are located at the center of laser spot i.e., in the regions where the laser energy/fluence is highest ($F_{\text{Center}} = 215 \text{ mJ/cm}^2$).

AFM analyses were also performed on the CDG/YSZ laser irradiated samples as presented in Figure 4, for the samples corresponding to those imaged in Fig. 3. Figure 4.a corresponds to the sample irradiated with a low dose ($F = 125 \text{ mJ/cm}^2$ and $N = 50$) and confirms the formation of nano-squared structures with typical side length of $\sim 250 \text{ nm}$ (in fair agreement with the SEM image, Fig. 3.a) with a depth amplitude varying between 20 and 40 nm. However, if we compare their shapes with that obtained at high energy dose (Fig. 4.b, $F = 310 \text{ mJ/cm}^2$ and $N = 1000$), we can notice that the size of the latter is

somewhat smaller (220-230 nm) with a slightly greater depth amplitude of about 50 nm. At the higher dose, some re-deposition is observed at the surface appearing as dispersed white spots in Fig. 4.b. The effect observed at the higher laser dose could be explained by the injection of photonic energy in the CDG/YSZ system.

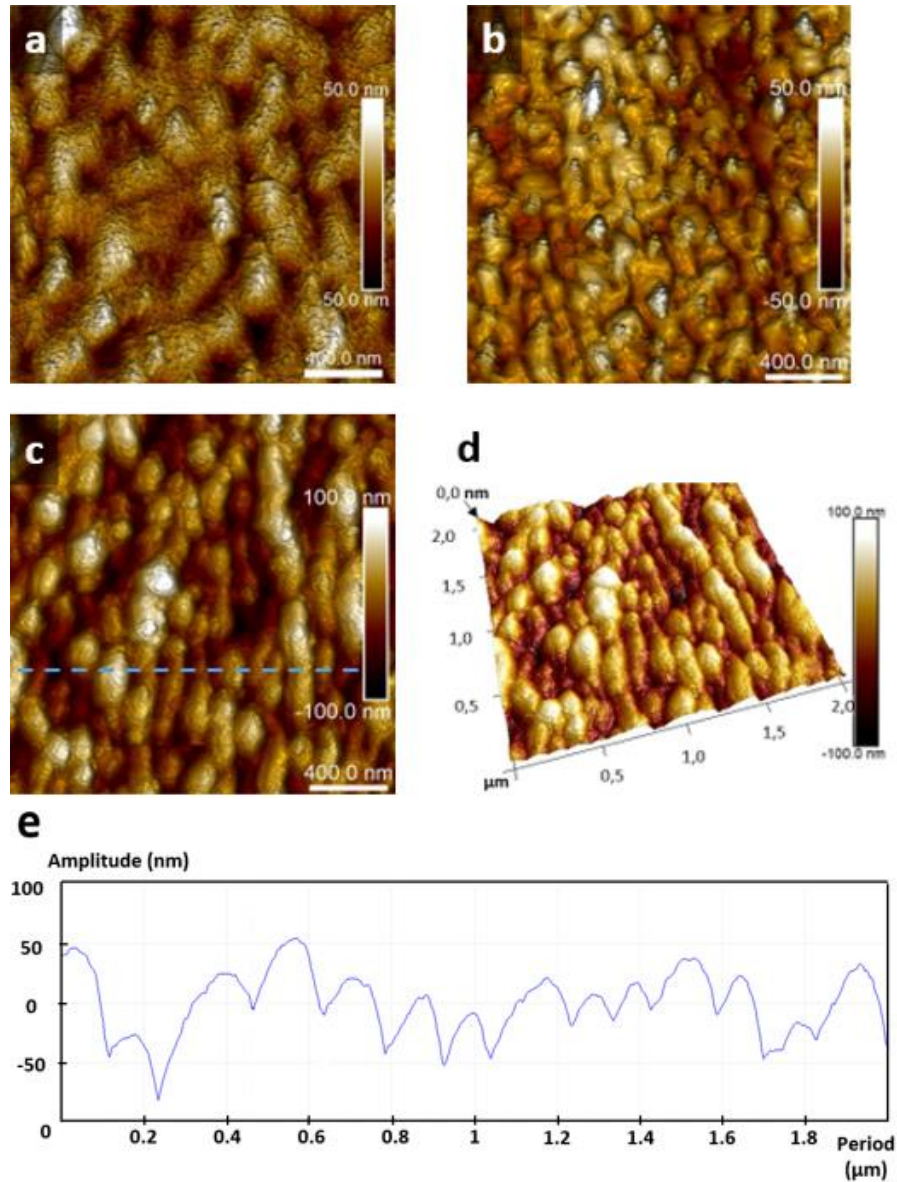


Fig.4 AFM height images (size $2 \times 2 \mu\text{m}^2$ size) show the topography of YSZ substrate after GDC ablation at low and high energy doses that's correspond: (a) Fig.3-a at $F = 125 \text{ mJ/cm}^2$ and $N = 50$; (b) Fig.3-b1 and (c, d, e) Fig.3-b2 for $F = 310 \text{ mJ/cm}^2$ and $N = 1000$; (e) shows the evolution of the period and amplitude of HSFL structures generated along a measurement profile.

Furthermore, Figure 4.c represents the AFM analysis of the periodic structures identified as HSFL in Fig.3.b2, which are formed in the center of the high fluence laser region within the laser spot (high laser dose conditions, $F = 310 \text{ mJ/cm}^2$, $N=1000$). A 3D view AFM image for this same irradiation condition is shown in Figure 4.d, which allows to visualize the profile of these ripples, a plot of which is presented Figure 4.e. This latter figure shows that the average spatial period of the LIPSS is about 130 nm, close to the third of the laser wavelength ($\lambda/3$), in agreement with the SEM image presented in Figure 3.b2,

and an amplitude varying between 50 and 60 nm.

The NS that appear on the YSZ surface after the complete ablation of GDC, can be a result of surface micro-cracking or fragmentation. It is generally accepted that these types of morphologies occur because of thermo-elastic stresses induced by the heating of the laser irradiated volume of the material [15,34]. Indeed, such structures were also observed by Talbi *et al.* in 1D patterns on the surface of TiO_{1.8} irradiated by a femto-second laser, when the laser fluence exceeds a damage threshold related to the cracking phenomenon before the melting phase [36]. Finally, the HSFL structures (spatial period close to 130 nm) formed under the high laser energy dose conditions (see Figure 3.b2) are attributed to a self-organization mechanism resulting from thermo-capillary and hydrodynamic instabilities as recently reported in the literature [35].

For comparative reasons, we have performed laser irradiation on the YSZ samples coated with a metallic gold thin film of 20 nm. For a laser fluence ($F = 250 \text{ mJ/cm}^2$), we vary the number of pulses from 1 to 1000 shots. Firstly, strong ablation occurs for the Au/YSZ film at the first laser shot as shown by the nanometric particles dispersed on the surface (Figure 5.a). By increasing N up to 10 pulses, most of the gold nanoparticles are removed from the surface with some cracking and melting of the surface occurring (Figure 5.b). At N=100 shots (Fig. 5.c), LIPSS formation is initiated, and those become well organized and resolved for N =1000 shots (Fig. 5.d). These ripples are LSFL-like, perpendicular to the E polarization with a spatial period close to 250 nm. We propose that the presence of the thin metallic film (Au) on the surface of YSZ, has contributed to enhance the excitation of the surface plasmon polaritons (SPPs) surface waves to interfere with the incident laser beam, as supported by the Sipe electromagnetic model for LSFL formation [37-39]. This excitation enhances the regularity of LIPSS formation on YSZ. It is noteworthy that we did not detect the appearance of NS structures for gold coated YSZ, as was the case for the GDC/YSZ system.

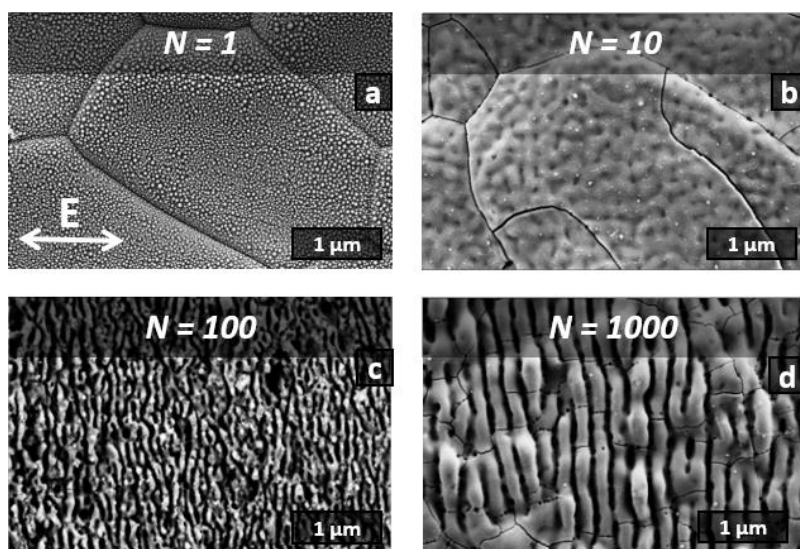


Fig.5 SEM images showing the evolution of Au/YSZ surface morphology as a function of N, for $F = 250 \text{ mJ/cm}^2$.

Indeed, the GDC dielectric layer is transparent at the wavelength used (355 nm), and therefore the laser photons will attack the surface of the YSZ substrate since the first laser pulse, which may explain the appearance of NS on YSZ just after complete removal of GDC. On the other hand, the mediated gold metallic layer will absorb the maximum laser photons.

2. Laser structuring of bare YSZ surfaces

Figure 6 shows SEM images of different morphologies at different location of the bare YSZ surface, irradiated under static mode conditions with 500 shots at a fluence of 310 mJ/cm^2 . Compared to the fluence $F = 250 \text{ mJ/cm}^2$ applied to the YSZ surface assisted by a gold thin film, necessary for LIPSS formation, the fluence value used in the case of direct texturing on YSZ was increased by about 20%. Indeed, Wen et al [40] reported that the threshold fluence of uncoated sapphire was 56% greater compared to Au-coated sapphire. Figure 6 shows three different laser-matter interaction areas, depending on the Gaussian distribution of laser beam (indicated by the dotted red line):

Zone I: The central ablation region that receives the highest amount of energy (peak intensity), showing a hole resulting from the ablation of the YSZ material, with the formation of micro-spikes at the hole boundary.

Zone II: Moving from the center to the edges, the intensity of the laser beam gradually decreases, we can assume that fusion of YSZ occurred with a texturing of the surface to form LIPSS (LSFL).

Zone III: At the edges of the laser impact, the lower energy density generates local changes through annealing of the YSZ substrate. This surface heating modifies the topography of the YSZ surface with the formation of less resolved LSFL.

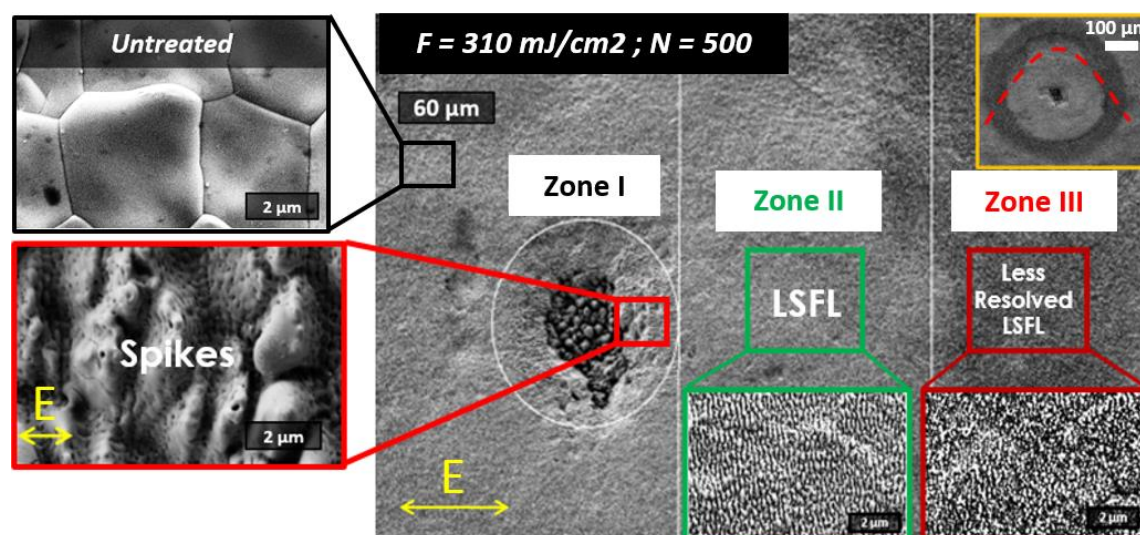


Fig.6 SEM image showing the three regions of the laser pattern formed on YSZ surface in static mode for $F = 310 \text{ mJ/cm}^2$ and $N = 500$: the white circle (ablation); the green box (melting); the red box (annealing); the black box (untreated sample of YSZ); as well as the yellow box showing the laser spot pattern on which we see the dotted line of the Gaussian profile of the picosecond laser beam of diameter $550 \mu\text{m}$.

In order to investigate the LIPSS formation domain directly on YSZ in static mode, the number of laser shots was varied between 100 and 1000 shots for two fluence values, 310 and 375 mJ/cm^2 . For $F = 310 \text{ mJ/cm}^2$, non-regular structures start to form on the YSZ surface, following the onset of local YSZ melting (Figure 7.a), but LSFL-like LIPSS are observed for 750 laser shots (Figure 7.b) with some local bifurcations appearing at the grain boundaries observed on the untreated YSZ sample. The large scale (micrometric) roughness of the YSZ grain morphology is preserved after laser texturing.

By increasing N up to 1000, we can observe poorly organized HSFL structures, also perpendicular to the polarization E (Figure 7.c). Indeed, L. Parellada-Monreal et al [41] reported HSFL textures of

period 145 nm with an amplitude of about 100 nm, on a zinc oxide (ZnO) sample using a femto-second laser at 800 nm. On the other hand, if we increase F up to 375 mJ/cm^2 , the formation of LSFLs starts rather after 100 shots. This confirms that the key parameter for LIPSS formation is the applied energy density (F) (Figure 7.d). The formation of HSFL occurs likewise when the number N of pulses increases from 750 to 1000 pulses (Figures. 7.e and 7.f).

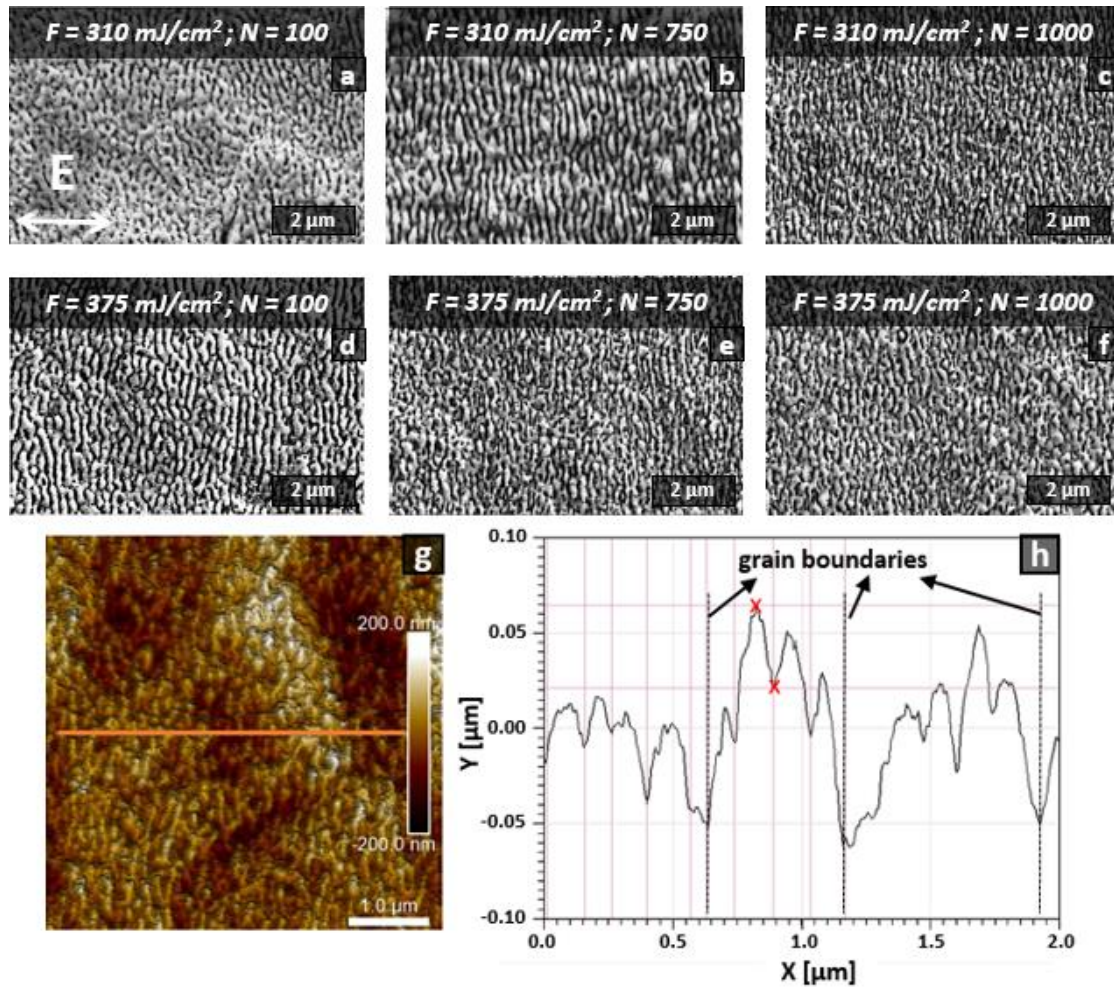


Fig.7 SEM image showing the LIPSS formation in static mode by varying the number of pulses from 100 to 1000 for two fluences $F = 310$ (a-c) and 375 mJ/cm^2 (d-f). (g) AFM height image ($5 \times 5 \mu\text{m}^2$ size) for the HSFL condition presented in (f), and (h) showing the period and amplitude evolution of the generated LIPSS along a measurement profile (orange line).

Figure 7.g shows an AFM image of the surface topography in static mode after laser irradiation of 1000 pulses at a fluence of 375 mJ/cm^2 . The profile analysis confirms that the average spatial period of the LIPSS formed is about 136 nm (Fig. 7.h), in agreement with the SEM image presented in Fig.7.f and an amplitude of about 40 nm.

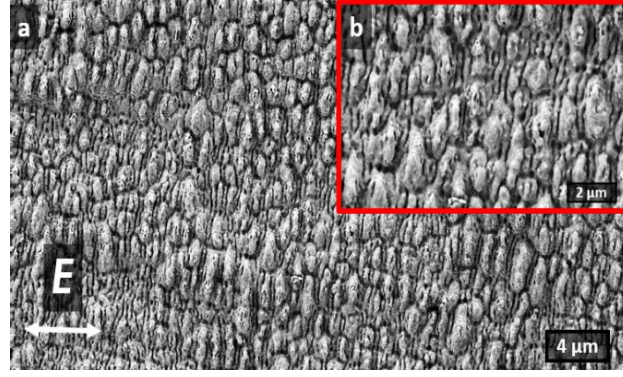


Fig.8 SEM images showing the LIPSS formation in static for $F = 310 \text{ mJ/cm}^2$ and $N = 20000$. (b) represents the magnification (x3) of the SEM image presented in (a).

In the case of a number of pulses $N = 20000$ at the same laser fluence ($F = 310 \text{ mJ/cm}^2$), elongated nano-spikes structures appear on top of the LSFL already formed on the YSZ surface, both of which are perpendicular to the polarization of the E laser beam, as shown in the figure 8. Based on SEM images, the size of these Nano-Spikes is found to vary between 0.8 and $1 \mu\text{m}$ (Figure 8.a), while the approximate spatial period of LSFLs is about 240 nm (Figure 8.b) [42].

The energy of a picosecond laser photon at 355 nm is 3.5 eV , which is much lower than the value of the YSZ band gap (5.8 eV), so it excludes the phenomenon of photoionization. Therefore, the YSZ substrate will not be ionized under the effect of few pulses laser regime, which explains the formation of LSFL for $N > 100$, as a result of laser shots accumulation effects [43].

Large surface LIPSS formation on the YSZ substrate was investigated under scanning mode conditions for a laser fluence of 310 mJ/cm^2 at different scanning speed from 30 to $6 \mu\text{m/s}$. For example, for a velocity of $6 \mu\text{m/s}$, the effective number of pulses " N_{eff} ", which is of the order of 4500 shots, is well outside the range of pulse values applied in the static mode ($100 < N < 1000$).

Table-1: N_{eff} versus scanning speed V_X applied for YSZ layer processing.

V_X ($\mu\text{m/s}$)	* $N_x = D \cdot f / V_X$ ($D = 550 \mu\text{m}; f = 10 \text{ Hz}$)	** $N_Y = D / \Delta Y$ ($\Delta Y = 100 \mu\text{m}$)	$N_{\text{eff}} = N_x \cdot N_Y$ (pulses)
30	184	5	920
20	275	5	1375
15	367	5	1835
6	917	5	4585

* N_x Effective number of pulses in X direction

** N_Y Effective number of pulses in Y direction

In Table 1, we report the different values of pulses N_x , N_Y and N_{eff} , for each scanning speed V_X . It can be noted that, the lower speed, the higher effective number, or in other words, the longer irradiation time of the laser beam. The objective is to structure a square of $4 \times 4 \text{ mm}^2$. The effective number $N_{\text{eff}} \approx 900$ shots, which corresponds to the velocity $V_X = 30 \mu\text{m/s}$, is likely to be almost correlated with what was observed in static mode for $F = 310 \text{ mJ/cm}^2$ and $N = 750$ shots (see Figure 7.b). With this condition shown in Figure 9.a, we observe periodic structures (LIPSS) on the YSZ surface. Going to a scanning speed of $V_X = 20 \mu\text{m/s}$ ($N_{\text{eff}} \approx 1375$), these ripples would become more regular since the energy dose

absorbed by the YSZ surface increased with the lowering of the velocity. For $V_x = 15 \mu\text{m/s}$ (Figure 9.c), material ablation due to the intense laser beam becomes more severe. On the other hand, an excessive decrease in scanning speed, accompanied by a significant rise in the YSZ surface temperature that exceeds the boiling temperature of YSZ, can lead to a phenomenon of complete evaporation of YSZ layer (thickness $8 \mu\text{m}$). Thus, we managed to find a range of parameters (F and V_x), to reproduce LIPSS in scanning mode to structure large-scale surfaces up to several mm^2 .

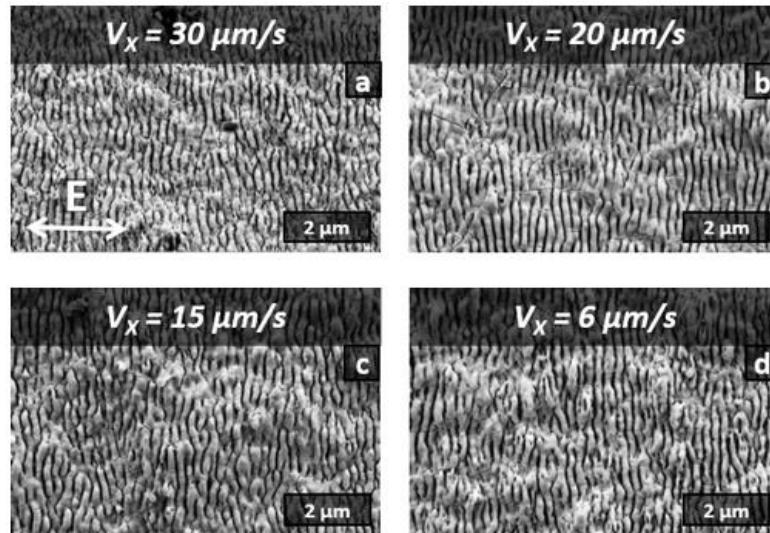


Fig. 9 SEM images showing the scanning conditions applied on the YSZ surface for $F = 310 \text{ mJ/cm}^2$.

An interesting phenomenon has been observed, when we irradiated YSZ with the picosecond laser beam at relatively higher fluences, $F = 625 \text{ mJ/cm}^2$, and $V_x = 0,1 \text{ mm/s}$, is a darkening (or blackening) effect [44] [45] as observed at the macroscopic scale on our sample i.e. the green surface color of YSZ is transformed into dark gray (Figure 10.a). According to Pereira et al. [46] and the work of Guo et al [47] this darkening effect could also be due to the loss of oxygen on the surface during laser irradiation.

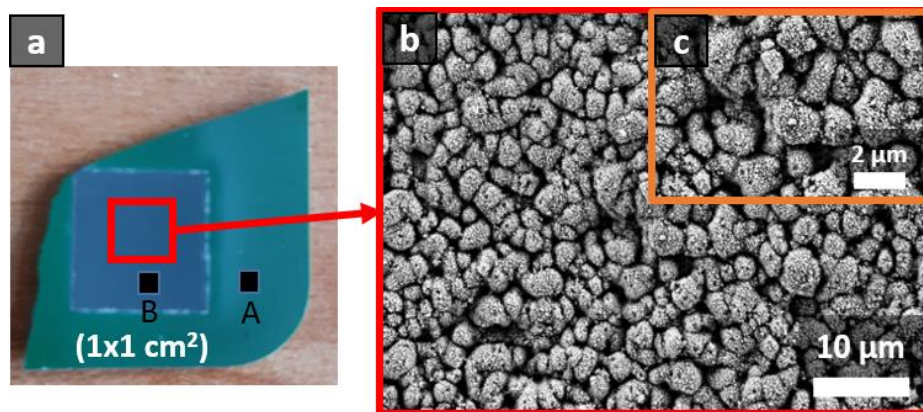


Fig. 10 (a) The blackening effect on the YSZ patterned by the picosecond laser beam at 355 nm , $F = 625 \text{ mJ/cm}^2$ and $V_x = 0,1 \text{ mm/s}$, (b) SEM image showing the appearance of micro-spikes upon the ablated YSZ surface and (c) the magnification ($\times 2$) of the SEM image presented in (b). The black squares (A and B) indicate the two DRX measurement points for the untreated and treated area of YSZ respectively.

In terms of morphology, this modification of the appearance is due to the formation of micro-Spikes on the laser structured YSZ surface having a size ranging from 1 to $4 \mu\text{m}$, as shown in Figures 10.b and 10.c.

On the other hand, this color variation has been noticed by Pereira [46] for several lasers textured YSZ samples (micro-grains, micro-cracks, etc.) for fluence ranging from 212 to 424 J/cm² and scanning speeds varying between 15 and 50 mm/s. On the cross-sectional SEM image of the textured YSZ (Figure 11), we can see that about half of YSZ thickness is ablated from the adjacent Ni-YSZ surface, confirming that the ablation threshold is reached at the high laser fluences leading to spike formation. Actually, the surface temperature increased to the evaporation temperature of the YSZ which explains the partial removal of the surface.

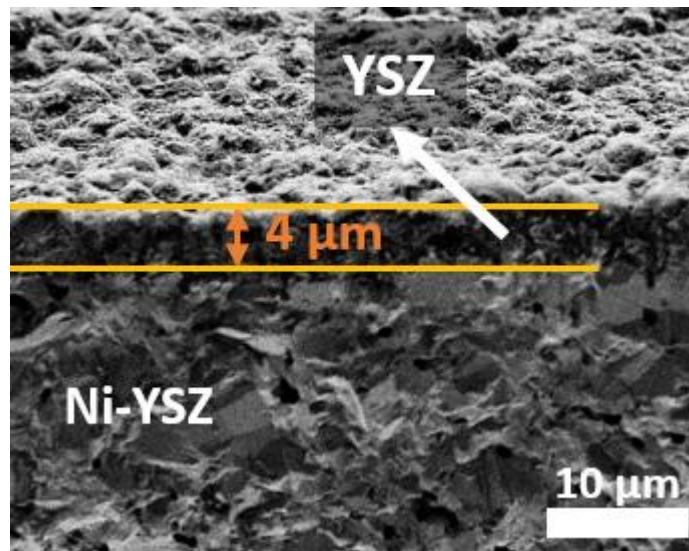


Fig.11 SEM image showing the cross section of YSZ material after laser texturing at $F = 625 \text{ mJ/cm}^2$, $V_x = 0.1 \text{ mm/s}$ and $\Delta Y = 0,1 \text{ mm}$.

X-ray diffraction (XRD) measurements were performed using the θ - 2θ method on two areas of the YSZ sample: Zone A (untreated) and Zone B (laser irradiated) to investigate the detected crystal phases. From the X-ray absorption coefficients of Y, Zr and O, we can estimate that 90% of the diffracted signal results from the 10-15 first micro-meters of YSZ surface. The observed crystallized phases are: Yttrium Stabilized Zirconia $\text{Y}_{0.15}\text{Zr}_{0.85}\text{O}_{1.93}$ (or 8YSZ), with a cubic phase $a = 0.514 \text{ nm}$ and face-centered-cubic phase of Nickel Oxide (NiO). For the untreated zone A, YSZ was predominant with a small trace of NiO (Figure 12.a). The position of the diffraction peaks is weakly shifted (0.1° approximately) towards the small angles, reflecting a lattice parameter ($a=0.516 \text{ nm}$) slightly higher than that expected for the 8YSZ phase ($a=0.514 \text{ nm}$). The film is well crystallized: The Full Width at Half Maximum “FWHM” is low (0.076°) indicating an average crystallite size of about 150 nm. However, for the zone B treated by laser, both YSZ and NiO were detected Figure 12.b.

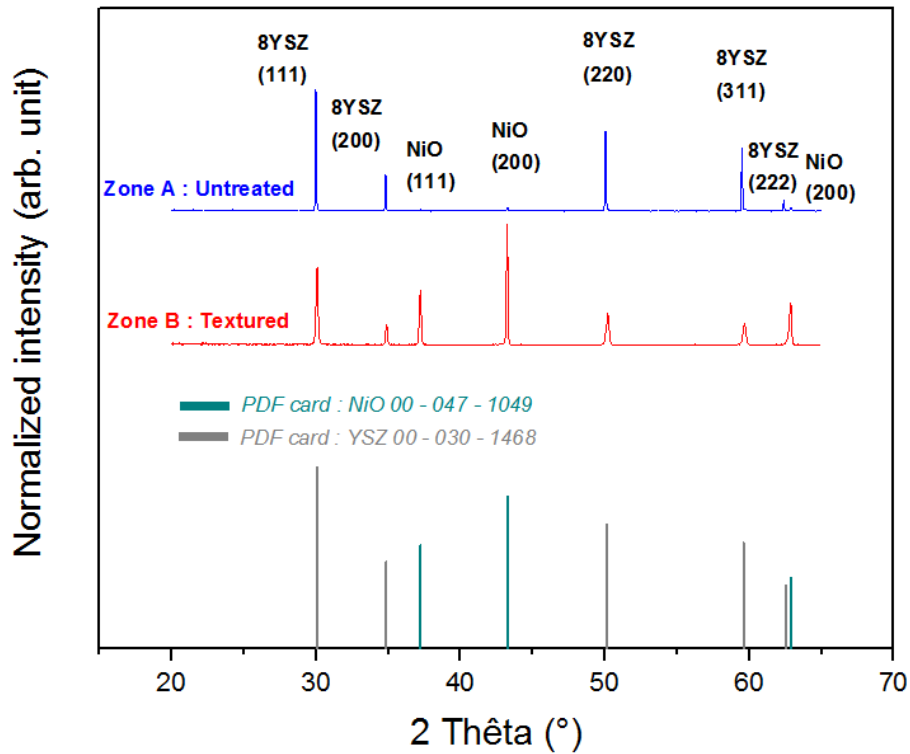


Fig.12 X-Ray Diffractometry on the YSZ film for both areas: untreated zone (a) and textured zone (b). $Y_{0.15}Zr_{0.85}O_{1.93}$ (8YSZ) material was retrieved from the database JCPDS file# 00-030-1468, and NiO from the database file# 00-047-1049.

The FWHM of the diffraction peaks is larger for the (111) YSZ peak, the FWHM is 0.166° which correspond to an average crystallite size of about 50 nm. Therefore, the darkening effect induced a lower YSZ crystallinity, i.e. a kind of disorder of the material. The position of the YSZ peaks is significantly shifted towards high angles. Indeed, the peak (111) is slightly shifted from 29.99° (before laser structuring) to 30.08° (after treatment), and the laser texturing induces a decrease of the lattice parameter of YSZ. Therefore, to maintain the microstructure of the YSZ required for the application, we should use laser fluences well below 625 mJ/cm^2 .

4. Conclusion

In this paper, we report on the fabrication of regular nanostructures on YSZ coatings and the feasibility to form LIPSS on microscale undulating YSZ surface via two experimental approaches: the first one consists in laser structuring of YSZ mediated through a thin film (dielectric "GDC" or metallic "Au"), while the second involves the direct structuring of a bare YSZ surface under static and scanning modes. The purpose of comparing the two laser structuring methods is to investigate the most regular LIPSS morphology that gives us a better increase in the specific surface area of the YSZ electrolyte exchange surface in solid oxide electrolyte cell (SOEC) applications. On the other hand, the formation of new structures like Nano-squares (NS) on YSZ by means of GDC thin film, can significantly increase the specific surface based on the geometrical model mentioned in our previous article cited in ref.32.

Firstly, in the mediated texturing of YSZ through a GDC oxide thin film, we have observed nano-squares structures on the YSZ surface after the complete ablation of GDC, under static mode for $F = 310 \text{ mJ/cm}^2$, $N = 1000$ at the edges of laser spot ($F_{\text{Edges}} = 150 \text{ mJ/cm}^2$). These NS (with a size of 250×250

nm²) resulted from thermo-elastic stresses induced by laser irradiation. Other HSFL structures, perpendicular to laser polarization, are observed at the center of the laser spot, and attributed to self-organization phenomena due to the accumulation effect of a high number of shots (N = 1000). These structures have a spatial period of about 120 nm. Uniform LSFL perpendicular to the laser beam polarization were formed on the YSZ substrate due to the excitation of the surface plasmon polaritons (SPP) waves. In the second part of the work, namely the case of laser irradiation of the bare YSZ surface, LSFL and HSFL structures were observed with an average spatial period measured for the thus-obtained HSFL is ~ 140 nm with an amplitude of 40 nm. We have also succeeded in reproducing LSFL on YSZ under scanning mode. Then, we have detected a darkening effect on YSZ samples, where micro-spikes microstructures are formed (size ~ 1 μm) for fluences exceeding 600 mJ/cm². Finally, XRD measurements demonstrated a slightly lower crystallinity of the laser irradiated YSZ material compared to the untreated YSZ surface.

Acknowledgments: The authors would like to thank the French ‘Region Centre-Val-de-Loire’ for funding via the ‘ARD Lavoisier’ and ‘ARD MATEX’ programs.

Conflicts of Interest: The authors declare no conflict of interest concerning this work.

References

- [1] K. Komeya, M. Matsui, High Temperature Engineering Ceramics, Book Chapter in Materials science and technology, Wiley-VCH Verlag GmbH & Co. KGaA, (2006). DOI: 10.1002/9783527603978.mst0126.
- [2] A. González, Study of the high-temperature behaviour of nanostructured coatings produced by thermal spraying (combustion and plasma) from powders and suspensions, PhD Thesis University of Limoges and Antioquia, Limoges (2014). <http://www.theses.fr/2014LIMO0046>.
- [3] G. Sreedhar, MD. M. Alam, V. S. Raja, Hot corrosion behaviour of plasma sprayed YSZ/Al₂O₃ dispersed NiCrAlY coatings on Inconel-718 superalloy, Surf. Coat. Technol 204 (3) (2009) 291-299. DOI: 10.1016/j.surfcoat.2009.07.026.
- [4] G. Kirmizidis, M. A. Birch, Microfabricated Grooved Substrates Influence Cell–Cell Communication and Osteoblast Differentiation In Vitro, Tissue Eng. Part A 15 (6) (2009) 1427-1436. DOI: 10.1089/ten.tea.2008.0137.
- [5] J. Y. Lim, H. J. Donahue, Cell Sensing and Response to Micro- and Nanostructured Surfaces Produced by Chemical and Topographic Patterning, *Tissue Eng.* 13 (8) (2007) 1879-1891. DOI: 10.1089/ten.2006.0154.
- [6] H. Hidalgo, A.-L. Thomann, T. Lecas, J. Vulliet, K. Wittmann-Teneze, D. Damiani, E. Millon, P. Brault, Optimization of DC Reactive Magnetron Sputtering Deposition Process for Efficient YSZ Electrolyte Thin Film SOFC, Fuel Cells 13 (2) (2013) 279–288. DOI: 10.1002/fuce.201200125.
- [7] P. Coddet, A. Caillard, J. Vulliet, C. Richard, A. –L. Thomann, Multistep magnetron sputtering process and in-situ heat treatment to manufacture thick, fully oxidized and well crystallized YSZ films, Surf. Coat. Technol., 349 (2018) 133-143. DOI: 10.1016/j.surfcoat.2018.01.079.
- [8] P. Coddet, M.-L. Amany, J. Vulliet, A. Caillard, A.-L. Thomann, YSZ/GDC bilayer and gradient barrier layers deposited by reactive magnetron sputtering for solid oxide cells, Surf. Coat.

- Technol., 357 (2019) 103–113. DOI: 10.1016/j.surfcoat.2018.05.065.
- [9] F. Chambetta, Characterization and development of a controlled sequential etching process at the nanoscale, PhD Thesis of Grenoble University (2018). <https://tel.archives-ouvertes.fr/tel-01873505>.
- [10] M. G. Holthaus, L. Treccani, K. Rezwan, Comparison of micropatterning methods for ceramic surfaces, *J. Eur. Ceram. Soc.* 31 (15) (2011) 2809-2817. DOI: 10.1016/j.jeurceramsoc.2011.07.020.
- [11] J. Bonse, S. Hohm, S. V. Kirner, A. Rosenfeld, J. Kruger, Laser-Induced Periodic Surface Structures— A Scientific Evergreen, *IEEE J. Select. Topics Quantum Electron.* 23 (3) (2017). DOI: 10.1109/JSTQE.2016.2614183.
- [12] D. Dufft, A. Rosenfeld, S. K. Das, R. Grunwald, J. Bonse, Femtosecond laser-induced periodic surface structures revisited: A comparative study on ZnO, *J. Appl. Phys.* 105 (3) (2009). DOI: 10.1063/1.3074106.
- [13] S. Bashir, M. Shahid Rafique, W. Husinsky, Femtosecond laser-induced subwavelength ripples on Al, Si, CaF₂ and CR-39, *Nucl. Instrum. Methods Phys. Res. Sect. B Beam Interact. Mater. At.* 275 (2012) 1-6. DOI: 10.1016/j.nimb.2011.12.016.
- [14] C. Kunz, J. F. Bartolomé, E. Gnecco, F. A. Müller, S. Gräf, Selective generation of laser-induced periodic surface structures on Al₂O₃-ZrO₂-Nb composites, *Appl. Surf. Sci.* 434 (2018) 582-587. DOI: 10.1016/j.apsusc.2017.10.224.
- [15] P. T. Mannion, J. Magee, E. Coyne, G. M. O'Connor, T. J. Glynn, The effect of damage accumulation behaviour on ablation thresholds and damage morphology in ultrafast laser micro-machining of common metals in air, *Appl. Surf. Sci.* 233 (1-4) (2014). DOI: 10.1016/j.apsusc.2004.03.229.
- [16] E. O. Filatova, A. S. Konashuk, Interpretation of the Changing the Band Gap of Al₂O₃ Depending on Its Crystalline Form: Connection with Different Local Symmetries, *J. Phys. Chem. C* 119 (35) (2015) 20755-20761. DOI: 10.1021/acs.jpcc.5b06843.
- [17] C. Florian, E. Skoulas, D. Puerto, A. Mimidis, E. Stratakis, J. Solis, and J. Siegel, Controlling the Wettability of Steel Surfaces Processed with Femtosecond Laser Pulses, *ACS Appl. Mater. Interfaces* 10 (42) (2018) 36564–36571. DOI: 10.1021/acsami.8b13908.
- [18] O. Shavdina, H. Rabat, M. Vayer, A. Petit, C. Sinturel, N. Semmar, Polystyrene Thin Films Nanostructuring by UV Femtosecond Laser Beam: From One Spot to Large Surface, *Nanomaterials* 11 (5) (2021) 1060. DOI: 10.3390/nano11051060.
- [19] A. Talbi, P. Coddet, M. Tabbal, AL Thomann, E. Millon, A. Stolz, C. Boulmer-Leborgne, GM O'Connor, N Semmar, Comparative study of laser induced periodic surface structures formed on pulsed laser deposited and magnetron sputtered titanium oxide films, *Appl. Surf. Sci.* 476 (2019) 303-307. DOI: 10.1016/j.apsusc.2019.01.069.
- [20] A. Talbi, A. Stolz, E. Millon, C. Boulmer-Leborgne, N. Semmar, Nanostructuring of titanium oxide thin film by UV femtosecond laser beam: from one spot to large surfaces, *Appl. Surf. Sci.* 418 (2017) 425-429. DOI: 10.1016/j.apsusc.2017.02.033.
- [21] T. T. D. Huynh, N. Semmar, Dependence of ablation threshold and LIPSS formation on copper thin films by accumulative UV picosecond laser shots, *Appl. Phys. A* 116 (3) (2014) 1429-1435. DOI: 10.1007/s00339-014-8255-0.
- [22] T. T. D. Huynh, A. Petit, N. Semmar, Picosecond laser induced periodic surface structure on copper thin films, *Appl. Surf. Sci.* 302 (2014) 109-113. DOI: 10.1016/j.apsusc.2013.10.172.
- [23] A. Talbi, S. Kaya-Boussougou, A. Sauldubois, A. Stolz, C. Boulmer-Leborgne, N. Semmar, Laser-induced periodic surface structures formation on mesoporous silicon from nanoparticles

- produced by picosecond and femtosecond laser shots, *Appl. Phys. A* 123 (463) (2017) 1-7. DOI: 10.1007/s00339-017-1075-2.
- [24] A. Talbi, A. Petit, Amer Melhem, A. Stolz, C. Boulmer-Leborgne, G. Gautier, T. Defforge, N. Semmar, Nanoparticles based laser-induced surface structures formation on mesoporous silicon by picosecond laser beam interaction, *Appl. Surf. Sci.* 374 (2016) 31-35. DOI: 10.1016/j.apsusc.2015.09.003.
- [25] T. T. D. Huynh, N. Semmar, In situ probing of pulsed laser melting and laser-induced periodic surface structures formation by dynamic reflectivity, *Appl. Phys. A* 116 (3) (2017) 1429-1435. DOI: 10.1088/2051-672X/aa7d2e.
- [26] K. Yin, C. Wang, J. Duan, C. Guo, Femtosecond laser-induced periodic surface structural formation on sapphire with nanolayered gold coating, *Appl. Phys. A* 122 (834) (2016). DOI: 10.1007/s00339-016-0361-8.
- [27] P. Feng, L. Jiang, X. Li, W. Rong, K. Zhang, Q. Cao, Gold-film coating assisted femtosecond laser fabrication of large-area, uniform periodic surface structures, *Appl. Opt.* 54 (2015) 1314–1319. DOI: 10.1364/AO.54.001314.
- [28] Y. Liu, Y. Wang, M. Yang, Q. Wu, Z. Li, C. Zhang, J. Zhang, J. Yao, J. Xu, Deep-subwavelength ripples on the ZnO surface obtained via metal-film-assisted femtosecond laser processing, *Appl. Surf. Sci.* 573 (2022) 151576. DOI: 10.1016/j.apsusc.2021.151576.
- [29] C. Kunz, S. Engel, F.A. Muller, S. Graf, Large-area Fabrication of Laser-Induced Periodic Surface Structures on Fused Silica Using Thin Gold Layers, *Nanomaterials* 10 (1187) (2020). DOI: 10.3390/nano10061187.
- [30] A. V. Dostovalov, T. J.-Y. Derrien, F. Přeučil, T. Mocek, V. P. Korolkov, S. A. Babin and N. M. Bulgakova, The evidence of the role of surface plasmon polaritons in formation of femtosecond highly-regular laser-induced periodic structures on Cr films, *J. Phys.: Conf. Ser.* 1092 (012025) (2018). DOI: 10.1088/1742-6596/1092/1/012025.
- [31] D. Shuleiko, S. Zobotnov, M. Martyshev, D. Amasev, D. Presnov, V. Nesterov, L. Golovan and P. Kashkarov, Femtosecond Laser Fabrication of Anisotropic Structures in Phosphorus- and Boron-Doped Amorphous Silicon Films, *J. Materials* 15 (7612) (2022). DOI: 10.3390/ma15217612.
- [32] W. Karim, A. Petit, H. Rabat, M. Tabbal, A.-L. Thomann, N. Semmar, Picosecond laser beam nanostructuring of GDC thin films: exchange surface enhancement by LIPSS, *Appl. Phys. A* 128 (731) (2022). DOI: 10.1007/s00339-022-05866-6.
- [33] M. Mickan, P. Coddet, J. Vulliet, A. Caillard, T. Sauvage, A.-L. Thomann, Optimized magnetron sputtering process for the deposition of gadolinia doped ceria layers with controlled structural properties, *Surf. & Coat. Tech.* 398 (2020) 126095. DOI: 10.1016/j.surfcoat.2020.126095.
- [34] S. K. Das, H. Messaoudi, A. Debroy, E. McGlynn, R. Grunwald, Multiphoton excitation of surface plasmon-polaritons and scaling of nanoripple formation in large bandgap materials, *Opt. Mater. Express* 3 (10) (2013). DOI: 10.1364/OME.3.001705.
- [35] T. Q. Jia, H. X. Chen, M. Huang, F. L. Zhao, J. R. Qiu, R. X. Li, Z. Z. Xu, X. K. He, J. Zhang and H. Kuroda, Formation of nanogratings on the surface of a ZnSe crystal irradiated by femtosecond laser pulses, *Phys. Rev. B* 72 (12) (2005). DOI: 10.1103/PhysRevB.72.125429.
- [36] A. Talbi, N. Semmar, M. Tabbal, G. O.' Connor; P. Coddet, A.-L. Thomann, A. Stolz, C. Leborgne, E. Millon, Femtosecond laser irradiation of titanium oxide thin films: accumulation effect under IR beam, *Appl. Phys. A* 126 (5) (2020) 390. DOI: 10.1007/s00339-020-03568-5.

- [37] L. P. Rivera, D. Munoz-Martin, A. Chávez-Chávez, M. Morales, G. Gómez-Rosas, et C. Molpeceres, Subwavelength LIPSS formation on SS304 by picosecond laser irradiation under water confinement, *Mater. Sci. Eng. B* 273 (2021) 115393. DOI: 10.1016/j.mseb.2021.115393.
- [38] D. Zhao, N. Gierse, J. Oelmann, S. Brezinsek, M. Rasinski, Y. Liang, C. Linsmeier, H. Ding, Investigation of laser ablation features of molybdenum bulk for picosecond laser-based techniques in fusion devices, *Fusion Eng. Des.* 151 (2020) 111379. DOI: 10.1016/j.fusengdes.2019.111379.
- [39] M. Senegačnik, M. Hočevar, P. Gregorčič, Influence of processing parameters on characteristics of laser-induced periodic surface structures on steel and titanium, *Procedia CIRP* 81 (2019) 99-103. DOI: 10.1016/j.procir.2019.03.018.
- [40] Q.L. Wen, H.L. Wang, G.H. Cheng, F. Jiang, J. Lu, X.P. X, Improvement of ablation capacity of sapphire by gold film-assisted femtosecond laser processing, *Optics and Lasers in Engineering* 128 (2020) 106007. DOI: 10.1016/j.optlaseng.2020.106007.
- [41] L. Parellada-Monreal, I. Castro-Hurtado, M. Martínez-Calderón, L. Presmanes, G. G. Mandayo, Laser-induced periodic surface structures on ZnO thin film for high response NO₂ detection, *Appl. Surf. Sci.* 476 (2019) 569-575. DOI: 10.1016/j.apsusc.2019.01.115.
- [42] N. Semmar, A. Talbi, M. Mikikian, A. Stolz, A. Melhem, D. de Sousa Meneses, Microspikes formed on mesoporous silicon by UV picosecond laser irradiation, *Appl. Surf. Sci.* 509 (2020) 144820. DOI: 10.1016/j.apsusc.2019.144820.
- [43] A. Nakhoul et al, Self-Organization Regimes Induced by Ultrafast Laser on Surfaces in the Tens of Nanometer Scales, *Nanomaterials* 11 (4) (2021) 1020. DOI: 10.3390/nano11041020.
- [44] F. Baino, M. A. Montealegre, J. Minguella-Canela, C. Vitale-Brovarone, Laser Surface Texturing of Alumina/Zirconia Composite Ceramics for Potential Use in Hip Joint Prosthesis, *Coatings* 9 (6) (2019) 369. DOI: 10.3390/coatings9060369.
- [45] C.G. Moura, R. Pereira, M. Buciumeanu, O. Carvalho, F. Bartolomeu, R. Nascimento, F.S. Silva, Effect of laser surface texturing on primary stability and surface properties of zirconia implants, *Ceram. Int.* 43 (17) (2017) 15227-15236. DOI: 10.1016/j.ceramint.2017.08.058.
- [46] R. S. F. Pereira, C. G. Moura, B. Henriques, J. Chevalier, F. S. Silva, M. C. Fredel, Influence of laser texturing on surface features, mechanical properties and low-temperature degradation behavior of 3Y-TZP, *Ceram. Int.* 46 (3) (2020) 3502-3512. DOI: 10.1016/j.ceramint.2019.10.065.
- [47] Xin Guo, Yao-Qing Sun, Kun Cui, Darkening of zirconia: a problem arising from oxygen sensors in practice, *Sens. Actuators B Chem.* 31 (3) (1996) 139-145. DOI: 10.1016/0925-4005(96)80058-X.

List of Figures

Figure 1: SEM image showing the transverse section of the untreated YSZ material.

Figure 2: Schematics of indirect (a) and direct (b) structuring approaches for YSZ material.

Figure 3: SEM images showing the comparison of the indirect texturing of YSZ at $F = 125 \text{ mJ/cm}^2$ and $N = 50$ (a) and $F = 310 \text{ mJ/cm}^2$ and $N = 1000$ (b) laser energy dose. The green box (b1) corresponds to the edges and the red box (b2) corresponds to the center of laser spot presented in (b).

Figure 4: AFM images show the topography of YSZ substrate after GDC ablation at low and high energy doses that's correspond: (a) Fig.3-a at $F = 125 \text{ mJ/cm}^2$ and $N = 50$; (b) Fig.3-b1 and (c, d, e) Fig.3-b2 for $F = 310 \text{ mJ/cm}^2$ and $N = 1000$; (e) shows the evolution of the period and amplitude of HSFL structures generated along a measurement profile.

Figure 5: SEM images showing the evolution of Au/YSZ surface morphology as a function of N , for $F = 250 \text{ mJ/cm}^2$.

Figure 6: SEM image showing the three regions of the laser pattern formed on YSZ surface in static mode for $F = 310 \text{ mJ/cm}^2$ and $N = 500$: the white circle (ablation); the green box (melting); the red box (annealing); the black box (untreated sample of YSZ); as well as the yellow box showing the laser spot pattern on which we see the dotted line of the Gaussian profile of the picosecond laser beam of diameter $550 \mu\text{m}$.

Figure 7: SEM image showing the LIPSS formation in static mode by varying the number of pulses from 100 to 1000 for two fluences $F = 310$ (a-c) and 375 mJ/cm^2 (d-f). (g) AFM image for the HSFL condition presented in (f), and (h) showing the period and amplitude evolution of the generated LIPSS along a measurement profile (orange line).

Figure 8: SEM images showing the LIPSS formation in static for $F = 310 \text{ mJ/cm}^2$ and $N = 20000$. (b) represents the magnification (x3) of the SEM image presented in (a).

Figure 9: SEM images showing the scanning conditions applied on the YSZ surface for $F = 310 \text{ mJ/cm}^2$ by using the picosecond laser beam at 355 nm ($f=10 \text{ Hz}$).

Figure 10: (a) The blackening effect on the YSZ patterned by the picosecond laser beam at 355 nm at $F = 625 \text{ mJ/cm}^2$ and $V_x = 0,1 \text{ mm/s}$, (b) SEM image showing the appearance of microspikes upon the ablated YSZ surface and (c) the magnification (x2) of the SEM image presented in (a). The two small black squares (A and B) indicate the two DRX measurement points for the untreated and treated area of YSZ respectively.

Figure 11: SEM image showing the cross section of YSZ material after laser texturing for $F =$

625 mJ/cm², $V_x=0.1\text{mm/s}$ and $\Delta Y=0,1\text{ mm}$.

Figure 12: X-Ray Diffractometry on the YSZ film for both areas: untreated zone (a) and textured zone (b).

List of Tables

Table 1: N_{eff} versus scanning speed V_x applied for YSZ layer processing

